**THE EUROPEAN
PHYSICAL JOURNAL E**

Regular Article - Living Systems

Non-specific cargo–filament interactions slow down motor-driven transport

Joelle A. Labastide[1], David A. Quint[2,3,6], Reilly K. Cullen[1,4], Bryan Maelfeyt[2,3], Jennifer L. Ross[1,5,a], and Ajay Gopinathan[2,3,b]

[1] Department of Physics, University of Massachusetts, 710 North Pleasant Street, Amherst, MA 01003-9337, USA
[2] Department of Physics, University of California, Merced, 5200 North Lake Rd, Merced, CA 95343, USA
[3] NSF-CREST: Center for Cellular and Biomolecular Machines (CCBM), University of California Merced, Merced, USA
[4] Division of Basic and Translational Biophysics, Eunice Kennedy Shriver National Institute of Child Health and Human Development, NIH, Bethesda, MD, USA
[5] Department of Physics, Syracuse University, Crouse Drive, Syracuse, NY 13104, USA
[6] Lawrence Livermore National Laboratory, Livermore, CA 94550, USA

Abstract Active, motor-based cargo transport is important for many cellular functions and cellular development. However, the cell interior is complex and crowded and could have many weak, non-specific interactions with the cargo being transported. To understand how cargo-environment interactions will affect single motor cargo transport and multi-motor cargo transport, we use an artificial quantum dot cargo bound with few (~ 1) to many (~ 5–10) motors allowed to move in a dense microtubule network. We find that kinesin-driven quantum dot cargo is slower than single kinesin-1 motors. Excitingly, there is some recovery of the speed when multiple motors are attached to the cargo. To determine the possible mechanisms of both the slow down and recovery of speed, we have developed a computational model that explicitly incorporates multi-motor cargos interacting non-specifically with nearby microtubules, including, and predominantly with the microtubule on which the cargo is being transported. Our model has recovered the experimentally measured average cargo speed distribution for cargo-motor configurations with few and many motors, implying that numerous, weak, non-specific interactions can slow down cargo transport and multiple motors can reduce these interactions thereby increasing velocity.

1 Introduction

The survival and proliferation of all living organisms rely on critical molecular motor-based active transport processes occurring within the complex and dynamic cellular environment. Prior studies have shown that the cytoskeletal network acts as the highway system for the transport of macromolecular and vesicular cargo by enzymes called motor proteins [1]. The organization and function of the network depends on microtubule associated proteins and enzymes [2, 3]. When the network or transport by enzymes is disrupted, the result is disease states, birth defects, or even failure

This work is dedicated to Fyl's love of solving a good experimental mystery.

Joelle A. Labastide and David A. Quint have contributed equally to this work.

[a] e-mail: jlross@syr.edu (corresponding author)
[b] e-mail: agopinathan@ucmerced.edu (corresponding author)

to thrive for the organism [4, 5]. Specifically, disruptions in kinesin-1, the motor tasked with rapid, unidirectional anterograde transport using the microtubule network, have adverse effects on neuronal signal transduction [6] and are thus connected to neurodegenerative and neuromuscular diseases in humans [5]. Prior studies have elucidated kinesin's structure [7, 8], ATPase activity [9], force production during motility [10], and processivity properties in vitro [11–13]. Recent studies on kinesin-1 cargo-trafficking have revealed that single motors are easily derailed or impeded by obstacles such as microtubule defects and surface-binding proteins [14, 15], raising interesting and important questions about the cell's traffic control mechanisms. Cargo transport by multiple kinesin motors has been shown to be far less sensitive to path-based obstructions [16, 17], reducing the detachment frequencies and perhaps affording alternate pathways, which circumvent obstacles, indicating that motor number is a fundamental element of traffic control mechanisms.

Theoretical work aimed at understanding molecular motor-based intracellular transport covers a wide

range of cargo-motor configurations, cytoskeletal components, and geometries [18]. These range from studies that focus at the molecular level on microtubule-kinesin head interactions and motor stepping kinetics [19–21] to collective transport by multiple motors [22–31]. Studies of bulk transport at the cellular scale [32–39] usually model the transport process by considering the effects of filaments in a mean-field manner, giving rise to random intermittent ballistic phases when bound to filaments and diffusive phases when detached from filaments. When filament networks are explicitly modeled, it has been found that rebinding and trapping effects are important [40, 41] and on larger scales, network topology, defined by filament lengths, intersections and orientation/polarity, is an important determinant of cellular transport [40].

While some prior studies have focused on motor-network interactions, there has been relatively little work on illuminating cargo–filament interactions that are not motor-mediated. Cytoskeletal networks in live cells can be dense, presenting obstacles and steric hindrances. These have been recently studied in the context of cargo behavior at microtubule intersections [41–45], where the steric effects impact the probability of switching from one track to another. Both the cargo and local network organization can associate with many protein complexes in cells. These associated complexes may interact in many specific and non-specific ways via electrostatic and hydrophobic interactions. Such cargo-network interactions would directly couple mechanically back to motor dynamics, affecting network transport.

Given the tremendous importance of motor transport processes and their fundamental connection to human disease states, we still have much left to understand. Though cell biological work has the advantage of observing transport within the naturally crowded, dynamic, architecturally complex, and dense microtubule networks of the intracellular environment, transport characteristics cannot be confidently deconvolved from the work of other motors and proteins. For instance, many cargos, even artificially introduced cargos, will associate additional motor proteins like dynein, a retrograde transporter that frequently acts opposite kinesin-1. Intriguingly, several independent observations of transport of single cargos in live cells have shown increased transport speeds [46–50]. These studies have concluded the increase in speed is the result of multiple motors, at odds with both in vitro and theoretical results. These remarkable observations expose the need for deeper mechanistic understanding of the effects of multi-motor transport within the context of complex microtubule networks.

With the goal of understanding the mechanisms of how motors and cargos traverse complex cytoskeletal networks similar to those found in cells, we performed in vitro experimental studies on artificial cargos transported on reconstituted dense microtubule networks and complemented our measurements with computational modeling. In this paper, we specifically focused on quantifying the velocities of fluorescent quantum dot (QD) cargos carried by single (1:1) and multiple (1:10) attached kinesin-1 motors. We characterized the transport speed distributions using automatic two-dimensional (2D) particle tracking. Restricting our analysis to cargo trajectories on a single filament (no switching), we found that QD cargos move slower than single kinesin-1 motors, yet the velocity was recovered partially with by increasing the number of motors on the cargo ($\sim$ 5–10 motors).

To theoretically probe the mechanism that causes this difference, we implemented Brownian dynamics simulations of motor cargo transport on single microtubules in the presence of non-specific interactions modeled as local force traps, which accurately reproduced the experimental distributions and highlighted the speed increase in the 1:10 population. The combination of our experimental and computational results strongly suggest that multiple motors are able to passivate or provide a steric buffer to reduce non-specific microtubule-cargo interactions. These interactions can exert forces on cargos commensurate with kinesin's stall force and therefore encumber transport. Multiple motors can therefore lead to cargo trajectories with higher average velocities by reducing non-specific interactions that can trap cargos.

2 Results and discussion

In order to test the ability of cargos to transport within high-density microtubule networks, we first created dense microtubule networks using a crossed flow path experimental chamber (Fig. 1A) [16]. Microtubules were flowed in several times from each direction and bound to the cover glass using anti-tubulin antibodies. The network densities from sample to sample appeared similar. The uncertainty of the measurement was dominated by the resolution of the image, $\sim$ 300 nm. We found that the distribution is log-normal, as expected for bounded Gaussian distributions, with a median mesh size being 1.9 μm (Fig. 1B, C).

Artificial cargos were made from streptavidin-bound QDs incubated with biotinylated kinein-1 motors (560 amino acids) using a SNAP tag and biotinylated SNAP ligand (see methods). QDs were incubated with biotinylated SNAP-kinesin at a 1:1 ratio with few (1 on average termed "1:1") motors bound or 1:10 ratio to create cargos with many (5–10 on average termed "1:10") motors bound. QDs were used as cargos because they were especially bright for imaging in either epifluorescence or total internal reflection fluorescence (TIRF) microscopy (Fig. 2A, B). QDs were easy to track by hand or with automated tracking software (see methods, Fig. 2C–F).

Using our homemade automated software to track individual QDs with high spatial resolution, we were able to report both the instantaneous (frame-to-frame) and average speeds for each QD in the field of view (Fig. 2). A representative trajectory (Fig. 3A, B), was broken into instantaneous displacements (d_i) equal to

Fig. 1 Microtubule network methods and quantification. **A** Schematic of a cross flow chamber, indicating the directions of consecutive microtubule solution flow-throughs (yellow chevrons). **B** Example network of microtubules observed in the center of the chamber. Scale bar is 10 μm. **C** Histogram of the length between intersections within the networks used in this study. The distribution is a log-normal with a median of 1.9 μm (199 lengths measured). The uncertainty of the measurement was 300 nm, the resolution of our measurement
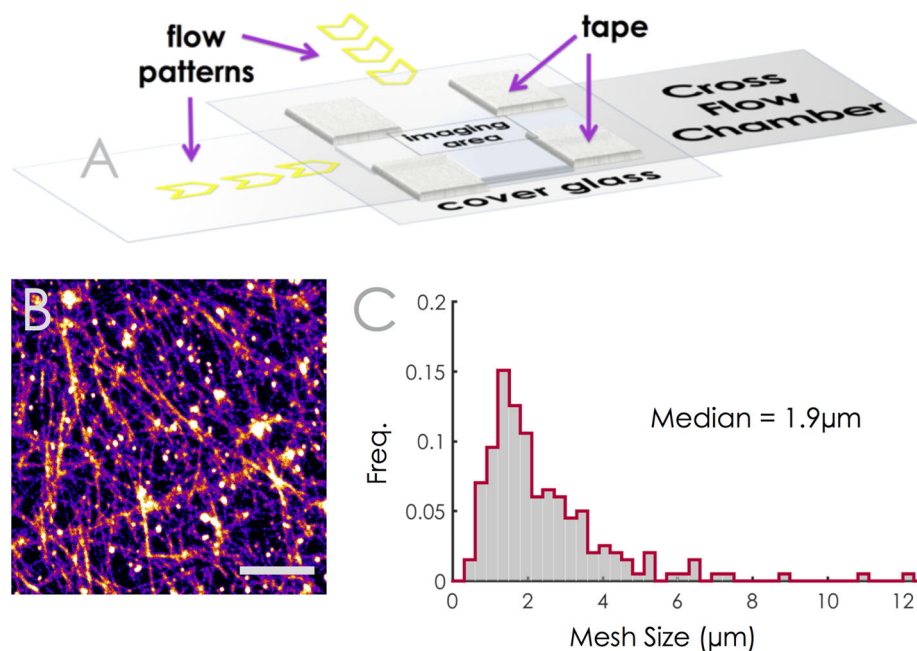
the distance traveled over each time step (δt_i), set by the experimental exposure time. The instantaneous speed, v_i, was the ratio of the instantaneous displacement and time step (Fig. 3B). For single GFP-kinesin motor on single microtubules, d_i were almost identical for the duration of the transport, resulting in a constant instantaneous speed over the motor's run (Fig. 3A, B). For cargos in dense networks, the d_i differed over the trajectory (Fig. 3C, D).

Using the automatically tracked trajectories, we also deduced the path length, defined as the sum of the instantaneous displacements. The path length divided by the total time of the trajectory yielded the average speed for the trajectory. We measured the total displacement, defined as the distance between the starting and ending positions of the trajectory. Using the path length and total displacement parameters, we quantified the tortuosity of the trajectory, defined as the ratio of the path length to the total displacement of the trajectory. While some trajectories of QDs through the network could turn and were highly tortuous, we focused our analysis on trajectories where the tortuosity was approximately equal to 1 (i.e., when the path length ~ displacement). We used these trajectories in order to avoid analyzing trajectories that may have traversed more than one microtubule. A separate study will examine trajectories with higher tortuosity to examine the effects of switching of microtubules on the transport process, but that is not the focus of this work.

2.1 Single motors with cargos interact with filaments

We quantified the average and instantaneous speeds (defined in the above section) of QD cargos with an average of one kinesin-1 motor ("1:1") or many (5–10) kinesin-1 motors ("1:10") and compared with the speeds of single molecule GFP-kinesin-1 motors (Fig. 4, Supp. Fig. S1). We found that the average speed distribution for single GFP-kinesin (Fig. 4A) was broad and roughly Gaussian, with a mode near 0.25 μm/s and a mean distribution speed of 0.38 μm/s. The mean kinesin speed we measured was in agreement with reports of kinesin's speed in the absence of cargo at saturating ATP concentrations (1 mM) [10]. The profile also fits with expectations of the distribution for average speeds for an unloaded motor [51].

The QD cargos with 1 kinesin (1:1) displayed a reduction in the average speed (0.19 μm/s) as well as an asymmetry in the distribution (Fig. 4B). Using the Kolmogorov–Smirnov test (KS-Test), we found that there was a less than 0.001% probability that the distribution for single GFP-kinesin and 1:1 QDs were the same (Supp. Table S1). The asymmetric non-Gaussian shape for the average speed distribution for QD cargos was surprising given that this is a distribution of averages, and, by the central limit theorem, we would expect it to tend to a normal distribution. Prior work has shown that processive motors with discrete steps under load, where the asymmetry increases with load, will display an exponential distribution [51]. Thus, this result suggests that the cargos are experiencing a load as they move. Comparing the GFP-kinesin to the 1:1 QDs indicates that the load acts to reduce the velocity of cargos, even when the cargos displaying the highest processivity and lowest tortuosity through the network are specifically selected. Since the viscous drag is minimal for a QD size cargo at these speeds, we expect that the load arises either from steric hindrance of the cargo due to nearby microtubules or specific/non-specific interactions between the cargo and nearby microtubules or perhaps a combination of the two.
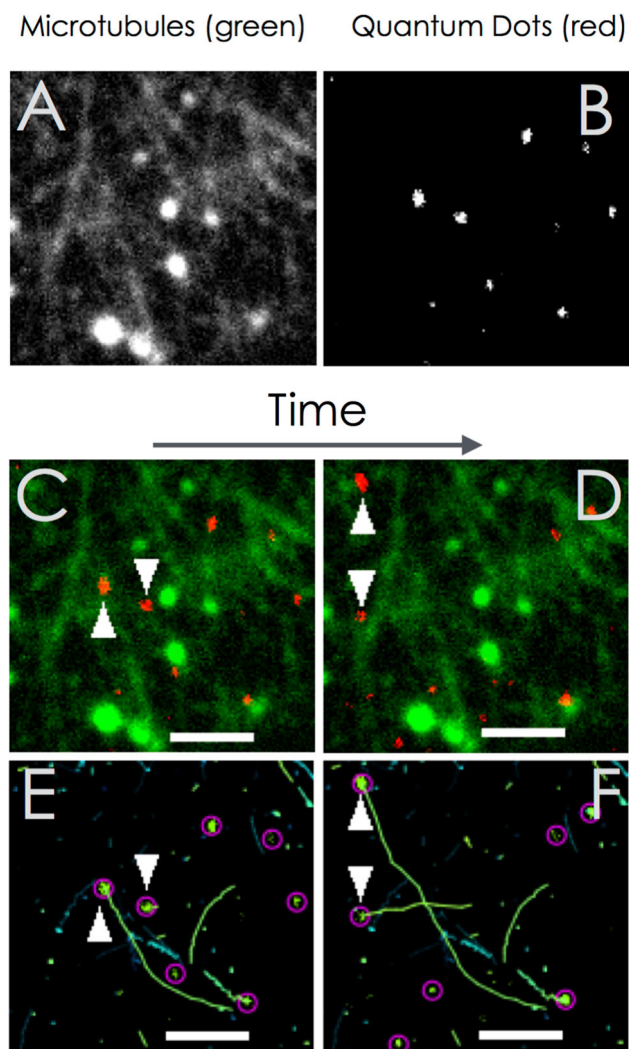
Microtubules (green)   Quantum Dots (red)

Time

Fig. 2 Example data for tracking QD cargo. **A** Example microtubule network. **B** Example image of quantum dots within the microtubule network in (**A**). **C** Overlay of microtubule network (green) from (**A**) and image of quantum dots (red) from (**B**) to show quantum dots bound to microtubules (arrowheads). **D** Image of same microtubule network (green) as (**A**, **C**) with quantum dots (red) at 5.8 s later. **E** High-resolution tracked quantum dots (magenta circles) trajectories (green lines) for a time series movie of quantum dot motility in the same location shown in (**A**) and (**C**). Arrowheads denote the same quantum dots from (**C**) (**F**). Trajectories (green lines) of the tracked QDs (magenta circles) at the same time point as (**D**). Arrowheads denote the same quantum dots. Scale bar is 10 µm for all images

We also performed the same measurement on cargos with up to 5–10 motors bound (1:10) and observed a recovery in the average speed distribution (average 0.23 µm/s) back to higher speeds when compared to the 1:1 cargos (Fig. 4C). This shift was shown to be statistically significant (KS-Test, Supp. Table S1). The recovery of the velocity was also clear in the rightward shift of the median of the distribution and the longer tail at higher average speeds. Given that the 1:10 QDs

have about the same size as 1:1 QDs and therefore subject to about the same steric hindrance (if not more), it is surprising that they can move faster. This result implies that the increased motor number must either overcome or negate the steric hindrance and/or specific or non-specific interactions with the microtubule network.

We also quantified the instantaneous speeds for single GFP-kinesin, 1:1 cargos, and 1:10 cargos. For all the experiments, the instantaneous speed displayed an exponential decay (Fig. 4D-F). The medians of these distributions were low due to a high number of instantaneous speeds that were zero. The means of the instantaneous speed distributions were highest for single GFP-kinesin (0.216 µm/s $\pm$ 0.002 µm/s), lowest for 1:1 cargos (0.084 µm/s $\pm$ 0.003 µm/s), and in the middle for 1:10 cargos (0.131 µm/s $\pm$ 0.004 µm/s); which is the same trend that is observed for the average speed distributions. These distributions are statistically distinct from one another, using the KS-Test (Supp. Table S1), with p values of $p < 0.001$ for all tests.

What could account for the interactions between the cargo and environment? Firstly, a single kinesin is different than a kinesin with a quantum dot because the quantum dot is coated with PEG polymers. Although these are advertised as "inert" polymers, PEG is known to weakly interact with many biological systems including with microtubules [66] and with urease enzymes [67]. Unbound His-Tags/streptavidin on the surface may also contribute to the interactions, though they are far too few (we estimate 0–1 in the vicinity of the microtubule) to result in the sustained interactions observed. Secondly, given the large distance between neighboring filaments (about 2 microns), encounters of the cargo with other filaments (including steric blockades) would be too infrequent to account for the observations. The cargo-MT interactions are thus likely dominated by the non-specific PEG mediated interaction with the microtubule track it is currently walking on.

We also see that the addition of more motors to the small cargo can partially recover and increase the speed by about 20%. The maximum force achievable due to the motors on the 1:10 QDs should be higher than 1:1 or single kinesin motors because each motor can add up to about 5 pN of force. In an unloaded situation, however, adding more motors typically does not increase the speed, since the velocity is not proportional to the force when there is very little drag. Prior reports have, in fact, demonstrated that teams of motors could actually reduce the speed [24, 52, 53]. This is especially true for kinesin motors that have been shown to be unable to mechanically coordinate when working in teams [54, 55]. This miscoordination results in reduced speeds, limited by the slowest motor in the team. Multiple motors could, however, effectively increase the overall speed in the presence of a substantial load (due to weak cooperativity [65]) and potentially enable the cargo to overcome barriers due to steric hindrance or interactions. In our case, it is also possible that additional motors "passivate" the QD surface to further reduce the load that might come from interactions. This could

Fig. 3 Example trajectories in space and time for single GFP-kinesin-1 and QD cargos. **A** Example trajectory of a single GFP-kinesin-1 motor traversing a microtubule in a sparsely distributed network of microtubules in two dimensions over time (color bar). **B** Magnification of the trajectory from (**A**) to show individual displacements, d_i, for each time interval, δt_i, which were used to find the instantaneous speed, v_i. **C** Example trajectory of a QD with 10 kinesin-1 motors bound traversing a dense network of microtubules in two dimensions over time (color). **D** Magnification of the trajectory from (**C**) to show individual displacements, d_i, for each time interval, δt_i
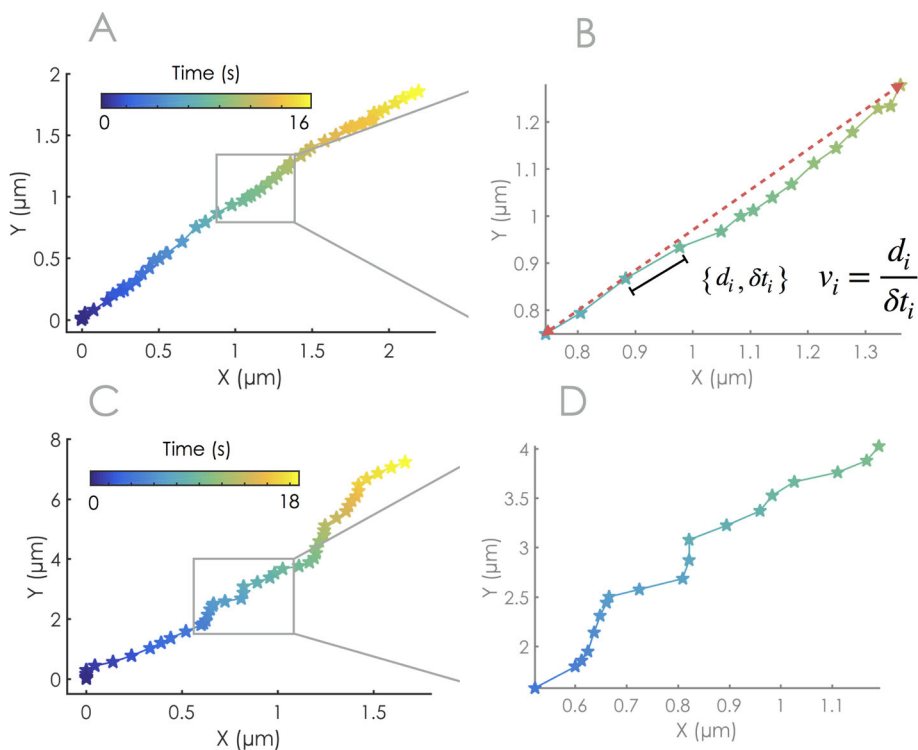
occur because the motors reduce the number of unconjugated streptavidin linkers on the QD surface (which might act as sites of filament-QD interactions—though this is unlikely to be significant given the low estimated number as pointed out above) and more significantly providing a physical steric buffer between the PEG QD surface and the filament it is being transported on.

2.2 Computational modeling

Given the experimental results demonstrating that QD cargos move slower than single motors, and that the speed can be partially rescued by adding more motors, we hypothesized that QD cargos have increased load due to interactions with the microtubule network and that adding more motors could reduce these interactions. To test our hypothesized mechanism, we implemented a Brownian dynamics simulation that allowed us to tune the interactions between the cargo and the environment and observe the effects on cargo speed. The simulated cargo's motion is described by one-dimensional, over-damped, Langevin dynamics governing $x(t)$, the cargo's position on the microtubule along which it is being transported:

$$x(t + \mathrm{d}t) = x(t) + \sqrt{D * \mathrm{d}t} * \eta + F/\xi * \mathrm{d}t \quad (1)$$

Here, D is the diffusion constant of the cargo accounting for Brownian noise, η is a normally distributed random variable, and ξ is the viscous drag coefficient of the QD due to the surrounding medium. Finally, F is the total force on the QD cargo arising from the

motors as well as any external forces due to interactions with the surrounding network. We use a standard model for the motors [53, 56, 61–64] with parameter values calibrated from experiment. Motors are modeled as one-sided springs with rest length L_{mot} and spring constant K_{mot}, exerting a force only under extension of $K_{mot}(L - L_{mot})$, where $L = |x_m - x|$ is the distance between the motor position on the MT, x_m, and the cargo position, x. The motor's position was advanced in each time step, dt, by a distance of $l = 8$ nm (step size of kinesin) with a probability of $1 - \exp(-v\mathrm{d}t/l)$, giving rise to an average motor speed of v. The average motor speed was taken to be load dependent, decreasing with increasing hindering (backward) force, F, as $v = v_0[1 - (F/F_s)^w]$, where v_0 is the unloaded motor speed, F_s is the kinesin stall force, and $w = 2$ [53, 56, 61–63]. The specific form of the relation chosen is not important as long as the values correspond to experimental calibrations.

While the cargo was transported, we proposed that it could non-specifically interact with the microtubule network. These interactions cannot be modeled by a constant force but rather as local interactions that are in effect only when the cargos are in the proximity of, and in particular orientations with respect to microtubules in the network (Fig. 5A). We considered that these interactions could locally trap the cargo, while the motors were free to continue to move on the microtubule and exert forces on the cargo (Fig. 5B).

To implement this effect in our simulation, we included force traps that were stochastically activated while the cargo was being transported. The trap activation frequency or trapping rate, Q_{trap}, was assumed

Average Speed Distribution

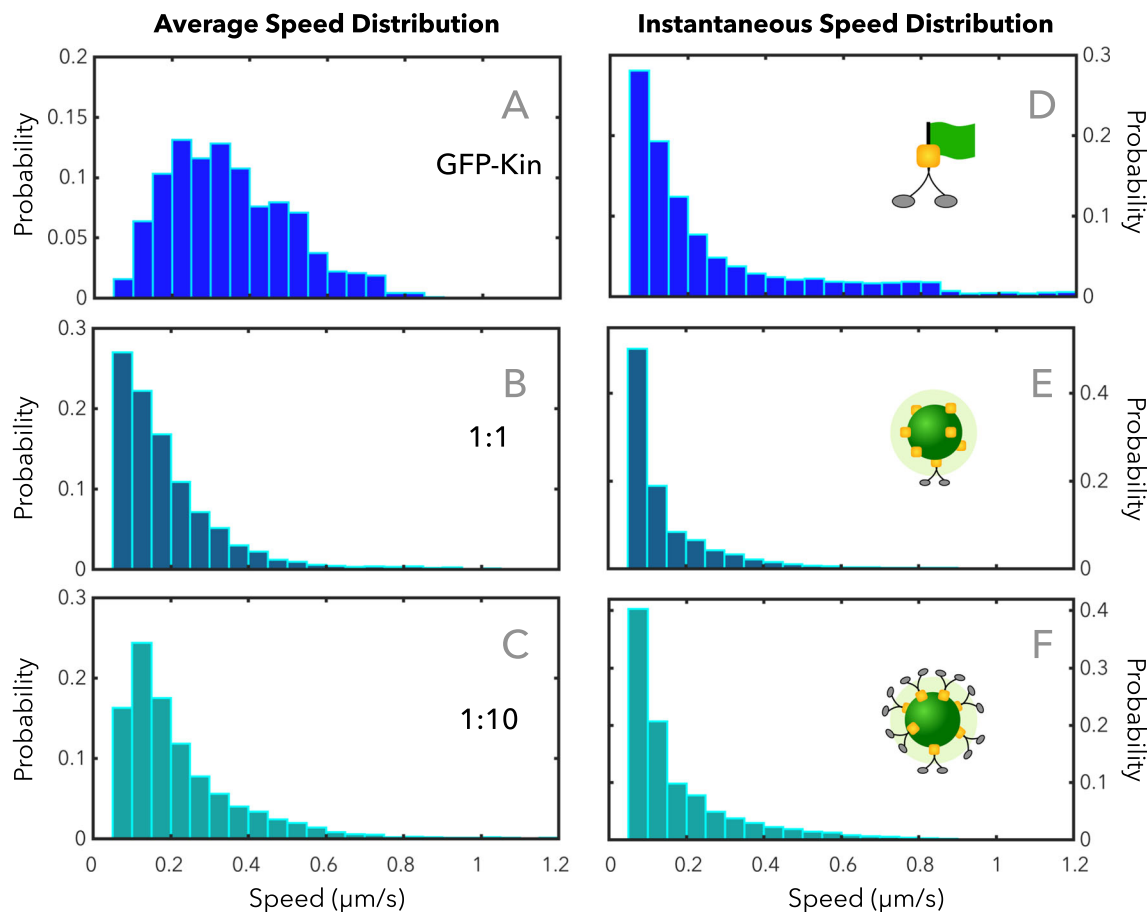## Instantaneous Speed Distribution

Fig. 4 Effects of instantaneous and average speed distributions when motors are loaded with cargo. **A** Normalized average speed histogram for GFP labeled kinesin (Sample size: $N = 959$). **B** Normalized average speed histogram for single motors attached to a QD (i.e., 1:1 configuration) ($N = 5614$). **C** Normalized average speed distribution for 1:10 configuration ($N = 8667$). **D** Normalized instantaneous speed distribution for single kinesin motors ($N = 2.0 \times 10^4$). **E** Normalized instantaneous speed distribution for 1:1 configuration ($N = 1.4 \times 10^5$). **F** Normalized instantaneous speed distribution for 1:10 configuration ($N = 2.6 \times 10^5$). Average speed distributions include data only from trajectories with total track displacement between 0.1 µm and 10 µm (to avoid stuck cargo and long tortuous trajectories). Averages for distributions in panel (**A**) and (**D**) are 0.348 µm/s $\pm$ 0.005 µm/s and 0.216 µm/s $\pm$ 0.002 µm/s, respectively. Averages for panels (**B**) and (**E**) are 0.190 µm/s $\pm$ 0.002 µm/s and 0.084 µm/s $\pm$ 0.003 µm/s, respectively. Averages for panels (**C**) and (**F**) are 0.232 µm/s $\pm$ 0.002 µm/s and 0.131 µm/s $\pm$ 0.004 µm/s, respectively. See Table S1 for more detailed statistics of all the distributions shown here

to be constant for a given QD cargo and represents the frequency with which the QD is positioned and oriented to interact with neighboring MTs. We modeled the force within the trap as arising from a Hookean spring with a spring constant, K_{trap} and equilibrium position, x_{trap} set by the position of the cargo at the instant the trap was activated. This allowed the cargo to move while trapped, but subject to an opposing force, $K_{\text{trap}}(x(t) - x_{\text{trap}})$, as the position of the cargo, $x(t)$, shifted away the equilibrium position of the trap. An example set of individual cargo trajectories, for QD cargo with 1 motor, is shown in Fig. 5B. It is to be noted that one trajectory exhibits a biphasic speed behavior with a slow, trapped phase arising from encountering

many force traps over an approximately 2 s long window during which the displacement was only 50 nm. Once the trap threshold force, F_{trap}, was reached and at least one motor was still attached to the microtubule, the QD could break free of the trap. Once free of the trap, the cargo was actively transported by the motors until the next trap was encountered. During each run of the simulation (maximum run time of $t_{\text{max}} = 100$ s), both the position of the cargo and the motors were recorded. For a complete list of simulation parameters and pseudo-code, please see the supplementary material Supplemental Figure S2 and Supplemental Table S2.

As a test, we ran our simulation for three values of the trapping rate, Q_{trap}, for 1 motor, with the unloaded
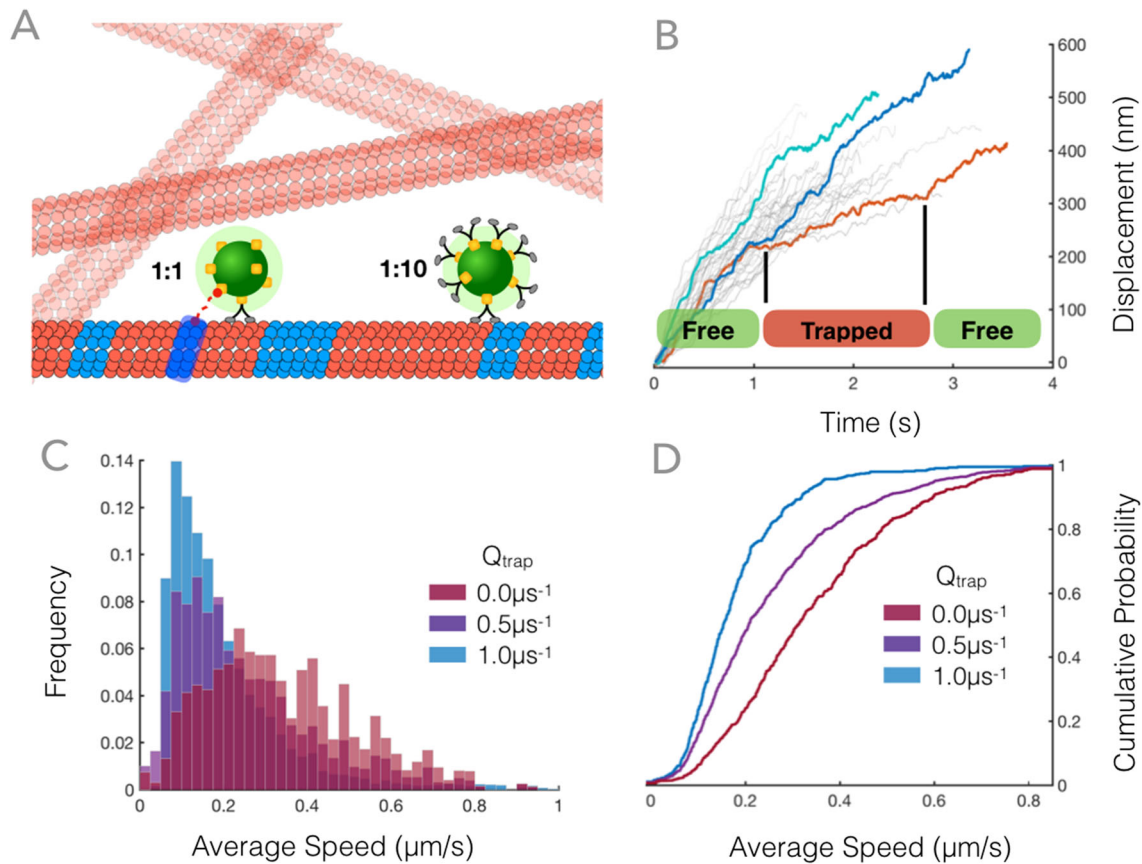
Fig. 5 A Illustration of QD network interactions. Microtubule (MT) network (red tubes) is randomly organized. Cargo spheres (green) are transported by kinesin motors (black/gray) along the microtubule network in two different configurations, 1:1 and 1:10. Cargo-MT interactions (force traps, blue MT sections) can stochastically occur between MTs and cargo with a frequency (trapping rate), Qtrap, that we hypothesize decreases with increasing motor number which passivate the QD. Interactions are modeled as force traps that exert Hookean forces (red-dashed line) on the cargo-motor system (**B**) Typical simulated cargo trajectories; highlighted (in color) tracks exhibit multi-phasic speed regimes where free travel is flanked by regions of slower average speed where the cargo is "trapped". **C** Average speed histograms for different values of the trapping rate Qtrap, produced by 103 simulated trajectories for each distribution. **D** Cumulative distributions of the histograms, clearly showing that the average speed increases for smaller values of Qtrap. Cargo in (**B**, **C**, **D**) has 1 motor

single motor kinesin speed, v_0 drawn from the experimentally measured GFP-kinesin average speed distribution (from Fig. 4A). We obtained three separate average speed distributions (Fig. 5C) from these simulations for 10^3 trajectories each, where each average speed is computed for one simulated trajectory. Figure 5C shows a systematic shift to higher average speed values as the trapping rate goes to zero. This is even more clearly visible in the cumulative distribution (Fig. 5D). The average speed distribution of the simulated data when the trapping rate was zero replicated the average speed distribution of the GFP-kinesin (compare Figs. 4A, 5C). This is as expected, given that the single motor speeds that form the basis of the simulation are drawn from the GFP-kinesin average speed distribution. When the trapping rate is increased, the distribution shifts to slower speeds with a median lower than the mean of the distribution (Fig. 5C). At very high trapping rate, the distribution appears shifted even more to lower speeds and drops rapidly for higher speeds as seen in both the probability and cumulative distributions (Fig. 5C, D).

2.3 Computational model fits to experimental data

We then set out to use the simulation generated average speed histograms (as in Fig. 5C) to quantitatively explain the experimentally measured average speed histograms (Fig. 4B, C). First, to gain further insight into the origins of the 1:1 and 1:10 average speed distributions we looked separately at short cargo runs (0.05–2.5 μm displacement) and long runs (> 2.5–10.0 μm displacement). We surmised that cargos that were subjected to force traps would have a greater chance of detaching as motors would experience higher opposing forces via the cargo and unbind. Therefore, those cargos would have shorter runs on average as well
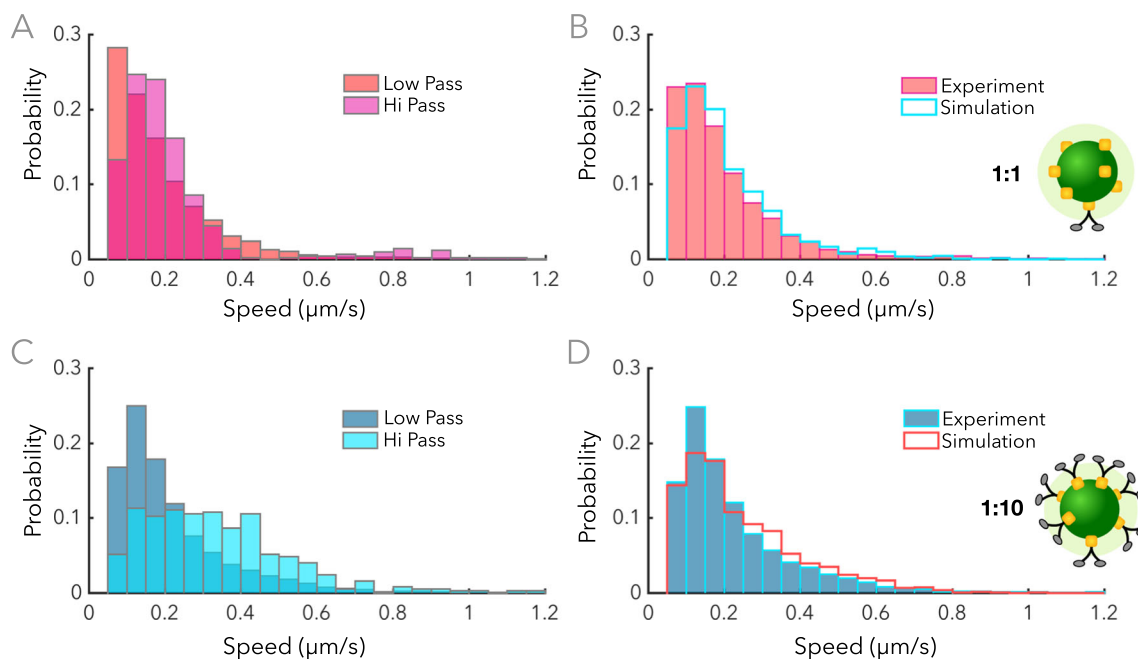
Fig. 6 Average speed histograms and simulation fits. **A** The average speed distribution for 1:1 data split into two sub-distributions based on total displacement that were short (low pass, 0.1–2.5 μm) and long (hi pass, 2.5–10.0 μm). **B** Simulation fit (cyan) of the 1:1 average speed distribution (pink). Best-fit parameter value was Ptrap = 0.2. **C** The average speed distribution for 1:10 data split into two individual normalized distributions that were short (low pass, 0.1–2.5 μm) and long (hi pass, 2.5–10.0 μm). **D** Simulation fitted 1:10 average speed distribution (red) with best-fit parameter value Ptrap = 0.4

as smaller average speeds. We plotted the average speed histograms for cargo trajectories that were short (low pass) and long (hi pass) for both the 1:1 (Fig. 6A) and 1:10 (Fig. 6C) cases. In the 1:1 case, we found that long and short runs both had similar speed histograms and the median speeds for both were surprisingly similar (Fig. 6A) with the long runs exhibiting a slightly larger fraction of high-speed trajectories. This indicated that for the 1:1 cargo configuration, the cargo was, for the most part, experiencing high loads and being slowed down.

The 1:10 speed distribution showed very different behavior (Fig. 6C). There were two distinct histograms for the short (low pass) and long (hi pass) cargo trajectories with median speeds that are separated by a significant amount. The longer trajectories, which displayed faster speeds, was similar to that for unloaded single GFP-kinesin, suggesting the dominance of configurations where the load was negligible. The slower (shorter run) subpopulation, on the other hand, had a speed distribution comparable to that of the slower distribution in the 1:1 configuration. These results suggest that the overall 1:1 and 1:10 speed histograms could be considered as different combinations of two distinct speed distributions arising from (i) impeded cargo under load (slower distributions in 1:1 and 1:10 cases) that experience force traps and (ii) unloaded cargo (faster distribution, most evident in 1:10 case) that do not experience force traps.

To determine the best combination of impeded and unloaded cargo speed distributions that fit the experimental results for 1:1 and 1:10 cargo configurations, we implemented the following procedure. We first simulated and generated speed distributions for two independent cargo-force trap scenarios, one where the trapping rate (Q_{trap}) is zero, and the other where the trapping rate is set to a finite value within a range (Supplementary Table 2). We seeded each simulation with motor speeds from the GFP-kinesin average speeds distribution (Fig. 4B). Speed distributions created for the 1:10 configuration were simulated with a maximum of two kinesin motors that could be actively engaged to accurately mimic the geometry of the situation. We deduced that this was the likely number available motors that could bind to the microtubule surface given the size of the QD and the average spacing of the motors on the QD surface.

We then created a composite average speed distribution given by a linear combination of the speed distribution with trapping rate, $Q_{\text{trap}} = 0 \, \text{s}^{-1}$, with weight P_{fit}, and the speed distribution with finite trapping rate, (here $Q_{\text{trap}} = 10^5 \, \text{s}^{-1}$), with weight 1-$P_{\text{fit}}$ (Fig. 7). After the composite distribution was created, we compared the cumulative distribution function (CDF) of the composite distribution to the CDF of the experimental speed distribution for each cargo configuration separately (Fig. 7B). We quantified the residual sum squared (RSS) between the composite CDF and the
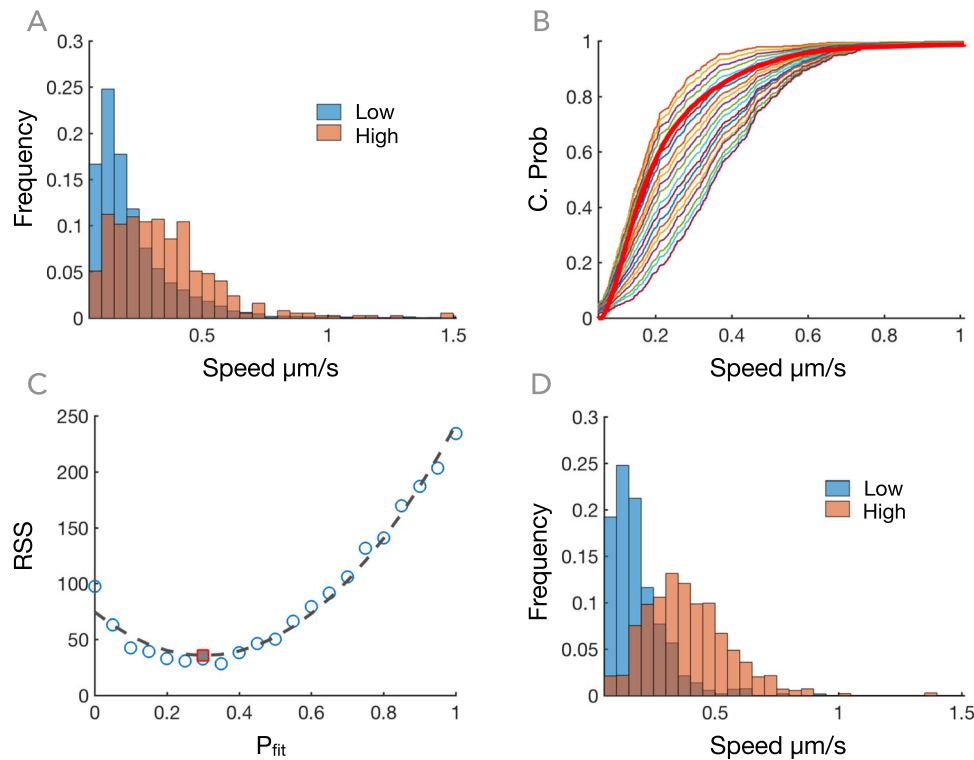
Fig. 7 A The 1:10 cargo configuration average speed distributions for short trajectories (low pass, 0.1–2.5 µm, blue) and long trajectories (high pass, 2.5–10 µm, brown). **B**. Simulated average speed distributions CDFs with different P_{fit} values plotted along with the experimentally measured 1:10 cargo configuration average speed distribution CDF (red). **C** The sum squared residual (RSS) of the simulated composite CDF against the experimentally measured 1:10 configuration CDF as a function of P_{fit}. The minimum indicates

the optimal value of P_{fit} that determines the best fit for the 1:10 average speed distribution. **D** The best-fit average speed composite distribution for 1:10 cargo configuration simulation data shows the same two sub-distributions for high (blue, $Q_{\mathrm{trap}} = 105$ s-1) and low (brown, $Q_{\mathrm{trap}} = 0$ s-1) trapping in the trajectories

experimentally measured CDF for each cargo configuration independently (shown for 1:10 configuration in Fig. 7C). The minimum of the RSS (Fig. 7C) provided the best-fit value of P_{fit} that best reproduced the overall average speed distribution. The sub-distributions for each best-fit simulated distribution were also in good qualitative agreement with the experimentally measured one (compare Fig. 7A, D). In physical terms, the parameter P_{fit} represents the probability that a particular QD cargo is non-interacting with the surroundings. We note that the cargo speedup we observe is predominantly due to the reduction in trapping rate as opposed to multiple motors pulling harder against load. This can be inferred because there was no statistically significant difference in the speed distributions between the $N = 1$ and $N = 2$ cases for similar trapping rates (compare Figs. 5C for single motor and 7D and 6D (sub-distributions not shown) for multiple motors) confirming that increased motors (2 in this case) cannot measurably speed up the cargo by exerting more force and/or pulling cargo out of traps.

Using the general method described above, we fit the simulated data to the experimental data for both the

1:1 and 1:10 cargos. We first set the finite trapping rate to a value $Q_{\mathrm{trap}} = 10^6$ s^{-1}, that, within a range (Supplementary Table 2), produced a good fit to the slower subpopulation speed distributions from the 1:1 and 1:10 cases ("low pass" distributions from Fig. 6A and C). We then simulated and fit our composite speed distribution to the experimental average speed distribution for the 1:1 configuration (Fig. 6B) and found the best-fit value for the weight of the unloaded, force trap free distribution ($Q_{\mathrm{trap}} = 0$) was $P_{\mathrm{fit}} = 0.2$. We repeated this method for the 1:10 cargo configuration, where the experimental speed distribution clearly had two separate sub-distributions (Fig. 6C). Here (Fig. 6D), we found the best-fit weight for the unloaded, force trap free distribution to be $P_{\mathrm{fit}} = 0.4$. These results indicated that the 1:1 QDs had an 80% chance of being impeded via interactions with the surroundings while the 1:10 QDs had only a 60% chance of being impeded.

Our simulation results show that the experimental speed distributions can be considered to arise from two subpopulations of cargo: one with impeded cargo that had interactions with the surrounding network and a slower speed and a second with unloaded cargo with

a faster speed (Fig. 6A, C). This was motivated by the fact that the 1:1 and 1:10 speed distributions both possessed a slow subpopulation of cargo speeds with approximately the same median, mode, and distribution of the speed (Fig. 6A, C "low pass"), but they had significantly different fast speed subpopulations (Fig. 6A, C "hi pass").

Our simulations were able to quantitatively recapitulate the average speed distributions we measure experimentally and also successfully captured the deviation found in the tails of the 1:1 and 1:10 speed distributions (Fig. 6B, D).

3 Conclusion

The study presented here represents a significant step toward closing the gap between in vitro studies of idealized cargo–motor–filament systems, which provide fundamental information outside of the physiological context, and in vivo studies with many, complex nonspecific interactions. It has been shown that motor proteins and cargos appear to go faster in live cells than the motors can go in vitro. We do see some speedup in our experiment aided by multiple motors, although we cannot recapitulate the increased speeds seen in live cells. Equally interestingly, previous studies comparing single to multi-motor cargo transport on single microtubules have shown differences in many characteristics of cargo transport but have not produced this speedup effect [16, 17, 56], raising still more questions about the plausibility and circumstances around the cooperation between motors. Most theoretical constructions result in multiple motors slowing down and gaining in run length, but not velocity, as more motors are added [56] though some speedup has been reported under load due to weak cooperativity [65].

Experimentally, we find that single kinesins move the fastest and adding a large cargo (QD) slows even a single kinesin, implying that the filaments are capable of interacting with the cargo and manifest as a load. Interestingly, the added load reduced when more motors were added. This is different from prior experimental measurements and theoretical models that mostly suggest that the inability of kinesin motors to cooperate causes multi-motor cargos to slow down—not speed up [24, 26, 31, 49, 54]. It is to be noted that we did not observe a slowdown with QD cargos in our previous work [17]. There, QD cargos were incubated with kinesin at the same ratio as our 1:1 case to begin with but the environment contained free kinesin that could bind to the MT as well as the cargo. This meant that the cargo was effectively being transported by multiple motors even at the lowest background concentrations of free kinesin. The similarity in speed between the cargo and GFP-single kinesin in that experiment is therefore consistent with our results in this paper where the addition of motors leads to a recovery of speed comparable to unloaded single motor speeds.

Guided by these observations, we proposed and tested a mechanism using computational modeling where the cargos transiently bound to the nearby microtubule via non-specific interactions during transport. These interactions were assumed to be stochastic, occurring when the cargo was in the proximity and able to interact with the filament and were strong enough to exert forces on the cargo commensurate with kinesin's stall force. Our results suggest that there are two subpopulations of cargo; one with impeded cargo that had interactions with the filament that moved slower; and a second, with essentially unloaded cargo that moved faster (comparable to GFP-kinesin). Cargo could therefore be characterized by the probability of being noninteracting or "inert", which our simulations showed to be directly connected with average transport speed. This non-interacting probability is a fitting parameter (P_{fit}) for the model and was able to capture the characteristics of our experimental speed distributions implying that this mechanism could explain our experimental results. In particular, the model also predicted systematic recovery of the unloaded speed when the non-interacting probability (P_{fit}) increased with increasing motor number, leading to the emergence of a second faster population in the speed histograms.

We believe the existence of two populations is due to the stochasticity in the number of motors on the QD due to the way they are prepared. The 1:1 case may have more than 1 motor while the 1:10 case may have anywhere from 5–10 motors available. This translates into both cases having cargo with a distribution of motor numbers available to bind simultaneously with the MT. In the low (1:1) motor density case, we expect the probability of having more than 1 motor to be low, while it will be higher in the 1:10 case. Having more than one motor could result in a significant reduction in the trapping rate as two or more motors can physically buffer the cargo PEG surface from interacting with the MT. Thus, the two populations likely correspond to cargos with one motor (interacting)) and those with multiple motors (non-interacting). The physical buffering of cargo–filament interactions by multiple motors leading to speedup is a novel feature highlighted by our work.

Given the complexity of the physiological environment, one might generically expect cargo to have many weak interactions with microtubules, which are reflected in our experimental set-up by non-specific PEG-MT interactions. Our results should therefore be relevant for the in vivo context and represent a springboard on which more complex investigations into intracellular transport traffic control may be launched.

4 Methods

Protein Purification A kinesin-1 construct truncated at amino acid 560 fused to either a carboxy-terminal SNAP tag (New England Biolabs) or GFP tag and a 6 × His tag were expressed using the pET-21(+) or pET17b

expression vectors, respectively. Expression with iso-propyl β-D-1-thio-galactopyranoside (IPTG) and affinity purification with nickel beads (Qiagen) were carried out as described previously [17, 57]. Additional affinity purification for SNAP-kinesin was performed through a bind and release to microtubules to remove truncated fragments of SNAP-kinesin that contained the SNAP tag, but not the kinesin motor. SNAP-kinesin or GFP-kinesin concentrations were quantified by comparison with known BSA standards on a Coomassie-stained SDS/PAGE gel.

Microtubule Preparation Rhodamine, DyLight 650, or Alexa-647 labeled microtubules were prepared using a 1:10 ratio of labeled/unlabeled tubulin. Rhodamine and DyLight 650 tubulin was purchased from Cytoskeleton. Alexa-647 labeled tubulin was purchased from PUR Solutions. Unlabeled tubulin was purified from porcine brain as described previously [58]. To prepare microtubules, both unlabeled and labeled tubulin were brought to 5 mg/mL in PEM-100 (100 mM K-PIPES, pH 6.8, 2 mM $MgSO_4$, 2 mM EGTA) and incubated for 10 min on ice. Tubulin was centrifuged at 4 °C for 10 min at 100,000 $\times$ g to remove tubulin aggregates. The remaining tubulin in the supernatant was mixed with 1 mM GTP and polymerized at 37 °C for 20 min. Taxol (50 μM) was added to stabilize polymerized microtubules, followed by another 20 min incubation at 37 °C to equilibrate the filaments. Polymerized microtubules were centrifuged at 25 °C for 10 min at 14,000 $\times$ g to separate unincorporated tubulin. The microtubule pellet was resuspended in PEM-100 with 40 μM Taxol.

Quantum Dot Cargo Assembly Quantum dots (QDs) decorated with single (1:1) or multiple (1:10) kinesin motors were prepared through incubation of QDs with different concentrations of biotin-SNAP-kinesin. Green-emitting QDs (520 nm), surface-functionalized with 5 to 10 streptavidin linkers, were purchased from Invitrogen and suspended in PEM-20 (20 mM K-Pipes, pH 6.8, 2 mM $MgSO_4$, 2 mM EGTA). SNAP-conjugated biotin ligands were added to each of two separate QD suspensions such that the ratios of QDs to ligands were 1:1 and 1:10, respectively, and incubated at room temperature for 20 min. Then, SNAP-tagged kinesin-1 was added to each of the solutions in amounts proportional to the biotin ligands and incubated for 4 h on ice, resulting in separate suspensions of QDs decorated with 1 and $\sim$ 10 kinesin motors, which we referred to as 1:1 and 1:10. The 1:10 QDs likely had 5–10 motors total on the QD, and only 2 motors could engage with the microtubule at a time during motility, due to the geometry of the motors attached to the QD [59].

Cargo Motility Assays Microtubule networks of high density were created using crossed flow chambers with perpendicular flow paths (Fig. 1A). Flow chambers were constructed from a silanized cover glass, double-stick tape, and a glass slide. Cover glasses were silanized to become hydrophobic by standard procedures, as previously published [17]. The glass surfaces of the chamber were cleaned with 70% ethanol and allowed to dry completely before being assembled. The chamber

was filled by flowing in and incubating a series of reagents in aqueous solution, replacing the entire internal chamber volume ($\sim$ 10 μL) with each new flow. We chose PEM-20, a low ionic strength PIPES buffer, as our working buffer for its ability to provide adequate pH control while minimizing dielectric screening of kinesin-microtubule interactions, thus increasing our data throughput.

The chamber was first flowed through with anti-tubulin (YL1/2 rat anti-α-tubulin) in PEM-20. We found that the concentration of tubulin antibodies helped to control the mesh size of the microtubule network where more antibodies allowed more microtubule to adhere. Next, a polymeric blocking agent (Pluronic F127, 5% in PEM-20) was used to reduce non-specific protein-glass interactions that cause background noise in the imaging plane. Next, a suspension of microtubules (labeled with 647 nm emitting Alexa-647 or DyLight 650 fluorophores) were flowed in and incubated along each axis of the crossed chamber. A PEM-20-Taxol solution (20 μM Taxol in PEM-20) was used to wash untethered microtubules out of the chamber. Microtubule networks were imaged using epi-fluorescence imaging to determine network density and stability prior to following in motors or QDs with motors.

Single- and multi-motor transport experiments were conducted in separate chambers prepared using the same method to produce comparable microtubule networks. Kinesin-decorated QDs were introduced to the network as part of a motility mix solution, which was flowed into the chamber on top of the microtubule network directly prior to imaging. The motility mix consisted of PEM-20, GFP-kinesin, 1:1, or 1:10 QDs, 1 mM ATP, reducing agent dithiothreitol (DTT) at 1 mM, a glucose oxidase (0.5 mg/ml), catalase (0.15 mg/ml), glucose (15 mg/ml) oxygen scavenging system, background concentrations of blocking agents Pluronic F127 (0.5%) and BSA (0.25 mg/ml), and the microtubule stabilizing agent, Taxol (20 μM).

Imaging Data were taken using a Nikon Ti-E inverted microscope with a 60x, 1.49NA objective and additional 2.5 $\times$ or 4 $\times$ magnification prior to projection onto the Ixon EM-CCD camera (Andor). The pixel size for these magnifications was 108 nm/pixel for 150 $\times$ or 67.5 nm/pixel for 240 $\times$ magnifications. The central regions of the crossed flow chambers were imaged for microtubule networks using epi-fluorescence (excitation/emission = 530 nm/647 nm). Microtubules were imaged at the beginning and end of each time series movie of QD transport to ensure that the networks remained stationary during kinesin transport. The QDs were imaged directly using a home-built total internal reflection fluorescence system built around the microscope body. Laser excitation was 488 nm and fluorescence emission 530 nm. Video microscopy with 10 ms exposures every 500 ms for a total of 5 min was recorded using the Nikon Elements software and saved a nd2 files as uncompressed tif files with meta data attached. Several videos were recorded on the same region of the

microtubule network to increase statistics within the same network. The video of the transport assay was superimposed on the picture of the microtubule network during post processing. Collapsing the movie stack of images by calculating the standard deviation of each pixel was used to correct for drift during imaging, since stationary particles in the background would all appear as lines in the standard deviation map.

Microtubule Network Measurements To measure the mesh size of the microtubule networks, we used the FIbeR Extraction (FIRE) algorithm [60] to extract information about the filament network from an image (Fig. 1B). FIbeR identified individual filaments that were composed of line segments connected at vertices, whose positions were recorded. By identifying the positions of intersections, which were vertices that are part of multiple filaments, we computed the distribution of distances between intersections (Fig. 1C).

Motility Data Analysis To properly quantify the 2D motion of QD or GFP labeled kinesin traffic on the microtubule network, we used automatic spot tracking software that is available for ImageJ/Fiji, called Trackmate [56]. Raw data (Fig. 2 A,B) and analyzed data with tracked QDs were highlighted with magenta circles with their trajectories are shown in green (Fig. 2 C-F). In any given set of QD image data, thousands of particles can be seen (Supplemental movie S1). Transient particles, such as those involved in non-processive binding and unbinding events, move in and out of the field of view rapidly and can still be tracked for a short time. We focused our analysis on cargos that remained in the field of view for longer than 1 s. These longer tracks displayed highly non-trivial trajectories, but for the purpose of this discussion, we have focused on the speed statistics (Fig. 3).

Using the extracted position and time data from the individual QD trajectories, we were able to calculate the instantaneous and average speed (speed in the case of unidirectional transport) distributions, for both the 1:1 and 1:10 motor cargo configurations (Fig. 4). To ensure selection of processive runs, the trajectories were filtered such that the maximum displacement, defined as the largest distance from the starting position achieved during that cargos track, exceeded our chosen threshold. The threshold was set to 0.4 μm. We parsed each track into a vector of instantaneous velocities, with each element (v_i) equal to the instantaneous displacement divided by the time step, and extracted an average speed v_{avg}, equal to the total path length over the total transit time.

Simulation Methods All simulation methods and parameters are given in the Supplemental methods.

Author contributions

JAL conceived and designed the work, performed data acquisition, analysis, and interpretation of data, drafted and edited the manuscript, and is accountable for the work. DAQ conceived and designed the work, performed simulations and theoretical calculations, analyzed and interpreted data, drafted and edited the manuscript, and is accountable for the work. JAL and DAQ contributed equally to the work. RKC helped with data acquisition, analysis, and interpretation of data. BM helped with data analysis and interpretation of data. AG conceived and designed the simulation work, analyzed and interpreted data, drafted and edited the manuscript, and is accountable for the work. JLR conceived and designed the experimental work, analyzed and interpreted data, drafted and edited the manuscript, and is accountable for the work.

Data availability Data sets generated during the current study are available from the corresponding authors on reasonable request.

Declarations

Ethical approval This study does not report experiments on live vertebrates and/or higher invertebrates. No animals were killed as part of this study.

References

1. J.L. Ross, M.Y. Ali, D.M. Warshaw, Cargo transport: molecular motors navigate a complex cytoskeleton. Curr. Opin. Cell Biol. **20**, 41–47 (2008)
2. R.D. Vale, The molecular motor toolbox for intracellular transport. Cell **112**, 467–480 (2003)
3. N. Hirokawa, Y. Noda, Y. Tanaka, S. Niwa, Kinesin superfamily motor proteins and intracellular transport. Nat. Rev. Mol. Cell Biol. **10**, 682–696 (2009)
4. N. Hirokawa, R. Takemura, Molecular motors and mechanisms of directional transport in neurons. Nat. Rev. Neurosci. **6**, 201–214 (2005)
5. E. Chevalier-Larsen, E.L. Holzbaur, Axonal transport and neurodegenerative disease. Biochimica et Biophysica Acta (BBA)-Mol. Basis Dis. **1762**, 1094–1108 (2006)

6. S.T. Brady, G.A. Morfini, Regulation of motor proteins, axonal transport deficits and adult-onset neurodegenerative diseases. Neurobiol. Dis. **105**, 273–282 (2017)

7. S. Rice, A.W. Lin, D. Safer, C.L. Hart, N. Naber, B.O. Carragher, S.M. Cain, E. Pechatnikova, E.M. Wilson-Kubalek, M. Whittaker, E. Pate, R. Cooke, E.W. Taylor, R.A. Milligan, R.D. Vale, A structural change in the kinesin motor protein that drives motility. Nature **402**, 778–784 (1999)

8. M. Kikkawa, Y. Okada, N. Hirokawa, 15 Å resolution model of the monomeric kinesin motor, KIF1A. Cell **100**, 241–252 (2000)

9. S.A. Kuznetsov, V.I. Gelfand, Bovine brain kinesin is a microtubule-activated ATPase. Proc. Natl. Acad. Sci. **83**, 8530–8534 (1986)

10. K. Svoboda, S.M. Block, Force and velocity measured for single kinesin molecules. Cell **77**, 773–784 (1994)

11. S.M. Block, L.S.B. Goldstein, B.J. Schnapp, Bead movement by single kinesin molecules studied with optical tweezers. Nature **348**, 348–352 (1990)

12. S.P. Gilbert, M.R. Webb, M. Brune, K.A. Johnson, Pathway of processive ATP hydrolysis by kinesin. Nature **373**, 671–676 (1995)

13. W.O. Hancock, J. Howard, Kinesin's processivity results from mechanical and chemical coordination between the ATP hydrolysis cycles of the two motor domains. Proc. Natl. Acad. Sci. **96**, 13147–13152 (1999)

14. W.H. Liang, Q. Li, K.M. Rifat Faysal, S.J. King, A. Gopinathan, J. Xu, Microtubule defects influence kinesin-based transport in vitro. Biophys. J. **110**, 2229–2240 (2016)

15. M.W. Gramlich, L. Conway, W.H. Liang, J.A. Labastide, S.J. King, J. Xu, J.L. Ross, Single molecule investigation of kinesin-1 motility using engineered microtubule defects. Sci. Rep. **7**(1), 44290 (2017)

16. J.L. Ross, H. Shuman, E.L.F. Holzbaur, Y.E. Goldman, Kinesin and dynein-dynactin at intersecting microtubules: motor density affects dynein function. Biophys. J. **94**, 3115–3125 (2008)

17. L. Conway, D. Wood, E. Tüzel, J.L. Ross, Motor transport of self-assembled cargos in crowded environments. Proc. Natl. Acad. Sci. **109**, 20814–20819 (2012)

18. P.C. Bressloff, J.M. Newby, Stochastic models of intracellular transport. Rev. Mod. Phys. **85**, 135 (2013)

19. F. Jülicher, A. Ajdari, J. Prost, Modeling molecular motors. Rev. Mod. Phys. **69**, 1269–1282 (1997)

20. R.D. Astumian, Thermodynamics and kinetics of a Brownian motor. Science **276**, 917–922 (1997)

21. M.E. Fisher, A.B. Kolomeisky, Simple mechanochemistry describes the dynamics of kinesin molecules. Proc. Natl. Acad. Sci. **98**, 7748–7753 (2001)

22. T. Guérin, J. Prost, P. Martin, J.-F. Joanny, Coordination and collective properties of molecular motors: theory. Curr. Opin. Cell Biol. **22**, 14–20 (2010)

23. M. Badoual, F. Julicher, J. Prost, Bidirectional cooperative motion of molecular motors. Proc. Natl. Acad. Sci. **99**, 6696–6701 (2002)

24. S. Klumpp, R. Lipowsky, Cooperative cargo transport by several molecular motors. Proc. Natl. Acad. Sci. **102**, 17284–17289 (2005)

25. M.J.I. Müller, S. Klumpp, R. Lipowsky, Tug-of-war as a cooperative mechanism for bidirectional cargo transport by molecular motors. Proc. Natl. Acad. Sci. U S A **105**, 4609–4614 (2008)

26. D.K. Jamison, J.W. Driver, M.R. Diehl, Cooperative responses of multiple kinesins to variable and constant loads. J. Biol. Chem. **287**, 3357–3365 (2012)

27. A. Kunwar, A. Mogilner, Robust transport by multiple motors with nonlinear force–velocity relations and stochastic load sharing. Phys. Biol. **7**, 016012 (2010)

28. A. Vilfan, E. Frey, F. Schwabl, Force-velocity relations of a two-state crossbridge model for molecular motors. Europhys. Lett. **45**, 283–289 (1999)

29. S. Leibler, D.A. Huse, Porters versus rowers: a unified stochastic model of motor proteins. J. Cell Biol. **121**, 1357–1368 (1993)

30. B. Geislinger, R. Kawai, Brownian molecular motors driven by rotation-translation coupling. Phys. Rev. E **74**, 011912 (2006)

31. F. Jülicher, J. Prost, Cooperative molecular motors. Phys. Rev. Lett. **75**, 2618–2621 (1995)

32. P. Bressloff, J. Newby, Directed intermittent search for hidden targets. New J. Phys. **11**, 023033 (2009)

33. A.V. Kuznetsov, A.A. Avramenko, D.G. Blinov, Numerical modeling of molecular-motor-assisted transport of adenoviral vectors in a spherical cell. Comput. Methods Biomech. Biomed. Engin. **11**, 215–222 (2008)

34. D.A. Smith, R.M. Simmons, Models of motor-assisted transport of intracellular particles. Biophys. J. **80**, 45–68 (2001)

35. C. Loverdo, O. Bénichou, M. Moreau, R. Voituriez, Enhanced reaction kinetics in biological cells. Nat. Phys. **4**, 134–137 (2008)

36. S.M.A. Tabei, S. Burov, H.Y. Kim, A. Kuznetsov, T. Huynh, J. Jureller, L.H. Philipson, A.R. Dinner, N.F. Scherer, Intracellular transport of insulin granules is a subordinated random walk. Proc. Natl. Acad. Sci. **110**, 4911–4916 (2013)

37. A. Kahana, G. Kenan, M. Feingold, M. Elbaum, R. Granek, Active transport on disordered microtubule networks: the generalized random velocity model. Phys. Rev. E **78**, 051912 (2008)

38. A.E. Hafner, H. Rieger, Spatial organization of the cytoskeleton enhances cargo delivery to specific target areas on the plasma membrane of spherical cells. Phys. Biol. **13**, 066003 (2016)

39. A.E. Hafner, H. Rieger, Spatial cytoskeleton organization supports targeted intracellular transport. Biophys. J. **114**, 1420–1432 (2018)

40. D. Ando, N. Korabel, K.C. Huang, A. Gopinathan, Cytoskeletal network morphology regulates intracellular transport dynamics. Biophys. J. **109**, 1574–1582 (2015)

41. M. Scholz, S. Burov, K.L. Weirich, B.J. Scholz, S.M.A. Tabei, M.L. Gardel, A.R. Dinner, Cycling state that can lead to glassy dynamics in intracellular transport. Phys. Rev. X **6**, 011037 (2016)

42. I. Goychuk, V.O. Kharchenko, R. Metzler, How molecular motors work in the crowded environment of living cells: coexistence and efficiency of normal and anomalous transport. PLoS ONE **9**(3), e91700 (2014)

43. K. Sozański, F. Ruhnow, A. Wiśniewska, M. Tabaka, S. Diez, R. Hołyst, Small crowders slow down kinesin-1 stepping by hindering motor domain diffusion. Phys. Rev. Lett. **115**, 218102 (2015)

44. G. Knoops, C. Vanderzande, Motion of kinesin in a viscoelastic medium. Phys. Rev. E **97**, 052408 (2018)

45. J.P. Bergman, M.J. Bovyn, F.F. Doval, A. Sharma, M.V. Gudheti, S.P. Gross, J.F. Allard, M.D. Vershinin, Cargo navigation across 3D microtubule intersections. Proc. Natl. Acad. Sci. U.S.A. **115**, 537–542 (2018)

46. C. Kural, Kinesin and dynein move a peroxisome in vivo: A Tug-of-War or coordinated movement? Science **308**, 1469–1472 (2005)

47. M.C. De Rossi, D.E. Wetzler, L. Benseñor, M.E. De Rossi, M. Sued, D. Rodríguez, V. Levi, Mechanical coupling of microtubule-dependent motor teams during peroxisome transport in Drosophila S2 cells. Biochimica et Biophysica Acta BBA General Subj. **1861**, 3178–3189 (2017)

48. C. Kural, A.S. Serpinskaya, Y.-H. Chou, R.D. Goldman, V.I. Gelfand, P.R. Selvin, Tracking melanosomes inside a cell to study molecular motors and their interaction. Proc. Natl. Acad. Sci. **104**, 5378–5382 (2007)

49. V. Levi, A.S. Serpinskaya, E. Gratton, V. Gelfand, Organelle transport along microtubules in *Xenopus* melanophores: evidence for cooperation between multiple motors. Biophys. J. **90**, 318–327 (2006)

50. D.B. Hill, M.J. Plaza, K. Bonin, G. Holzwarth, Fast vesicle transport in PC12 neurites: velocities and forces. Eur. Biophys. J. **33**, 623–632 (2004)

51. H.T. Vu, S. Chakrabarti, M. Hinczewski, D. Thirumalai, Discrete step sizes of molecular motors lead to bimodal non-Gaussian velocity distributions under force. Phys. Rev. Lett. **117**, 078101 (2016)

52. L. Scharrel, R. Ma, R. Schneider, F. Jülicher, S. Diez, Multimotor transport in a system of active and inactive kinesin-1 motors. Biophys. J. **107**, 365–372 (2014)

53. J. Xu, Z. Shu, S.J. King, S.P. Gross, Tuning multiple motor travel via single motor velocity: velocity control of travel distance. Traffic **13**, 1198–1205 (2012)

54. A.K. Efremov, A. Radhakrishnan, D.S. Tsao, C.S. Bookwalter, K.M. Trybus, M.R. Diehl, Delineating cooperative responses of processive motors in living cells. Proc. Natl. Acad. Sci. **111**, E334–E343 (2014)

55. E.L. Holzbaur, Y.E. Goldman, Coordination of molecular motors: from in vitro assays to intracellular dynamics. Curr. Opin. Cell Biol. **22**, 4–13 (2010)

56. J. Xu, S.J. King, M. Lapierre-Landry, B. Nemec, Interplay between velocity and travel distance of kinesin-based transport in the presence of Tau. Biophys. J. **105**, L23–L25 (2013)

57. D.W. Pierce, R.D. Vale, Single-molecule fluorescence detection of green fluorescence protein and application to single-protein dynamics. Methods Cell Biol. **1999**, 49–74 (1998)

58. J. Peloquin, Y. Komarova, G. Borisy, Conjugation of fluorophores to tubulin. Nat. Methods **2**, 299–303 (2005)

59. L. Conway, J.L. Ross, Measuring transport of motor cargos. Fluoresc. Methods Mol. Motors 235–52 (2014)

60. A.M. Stein, D.A. Vader, L.M. Jawerth, D.A. Weitz, L.M. Sander, An algorithm for extracting the network geometry of three-dimensional collagen gels. J. Microsc. **232**, 463–475 (2008)

61. A. Kunwar, M. Vershinin, J. Xu, S.P. Gross, Stepping, strain gating, and an unexpected force velocity curve for multiple-motor-based transport. Curr. Biol. **18**, 1173–1183 (2008)

62. N. Sarpangala, A. Gopinathan, Cargo surface fluidity can reduce inter-motor mechanical interference, promote load-sharing and enhance processivity in teams of molecular motors. PLoS Comput. Biol. **18**, 1–32 (2022)

63. J.O. Wilson, D.A. Quint, A. Gopinathan et al., Cargo diffusion shortens single-kinesin runs at low viscous drag. Sci. Rep. **9**, 4104 (2019)

64. C. Leduc, O. Campas, K.B. Zeldovich, A. Roux, P. Jolimaitre, L. Bourel-Bonnet et al., Cooperative extraction of membrane nanotubes by molecular motors. Proc. Natl. Acad. Sci. U.S.A. **101**(49), 17096–17101 (2004)

65. J.W. Driver, D.K. Jamison, K. Uppulury, A.R. Rogers, A.B. Kolomeisky, M.R. Diehl, Productive cooperation among processive motors depends inversely on their mechanochemical efficiency. Biophys. J. **101**(2), 386–395 (2011)

66. S. Sahu, L. Herbst, R. Quinn, J.L. Ross, Crowder and surface effects on self-organization of microtubules. Phys. Rev. E **103**, 062408 (2021)

67. M. Xu, J.L. Ross, L. Valdez, A. Sen, Direct single molecule imaging of enhanced enzyme diffusion. Phys. Rev. Lett. **123**, 128101 (2019)